

Atomic Quantum Sensor for Ultralow-Frequency Electric Field Measurements

Yu-Chi Chen, Shao-Cheng Fang, and Yi-Hsin Chen*

Department of Physics, National Sun Yat-Sen University, Kaohsiung 80424, Taiwan

(Dated: February 5, 2024)

Rydberg-assisted atomic electrometry with thermal vapors offers a promising approach for detecting external electric fields. This technique, however, has proven quite challenging for measuring low frequencies because of the effects of metal-alkali atoms absorbing on the interior surface of the vacuum enclosure. We apply high-contrast Rydberg-electromagnetically-induced-transparency (EIT) spectroscopy to investigate the impact systematically, including laser power and electric field. Our system enhances frequency measurements below 10 Hz, demonstrating significant progress in improving the performance of Rydberg atomic electrometry. Consequently, our study reveals a standard quantum limit for data capacity and experimentally illustrates it across bandwidths ranging from 10 Hz to 1 MHz. This study provides valuable insights for future precision measurements and field sensing applications.

I. INTRODUCTION

Highly-excited Rydberg atoms exhibit a substantial electric dipole moment, leading to significant polarizability and robust interactions with light [1–3]. Moreover, utilizing the dipole-dipole interaction (DDI) between Rydberg atoms can fine-tune the interactions among quantum bits, offering promising prospects for advancing quantum computing, including quantum gate operations [4, 5]. The combination of Rydberg interactions and electromagnetically induced transparency (EIT) allows for the realization of photon quantum gates [6–8]. Furthermore, the interaction strength between Rydberg atoms can be further enhanced through Förster resonance, achieved by applying external fields based on the Stark effect [9–15] with static fields [9–12], microwaves [13, 14], or optical fields [15].

Rydberg atomic electrometry provides a method for measuring electric-field-induced frequency shifts created by a Stark effect in high- n Rydberg resonances. Enhancing the sensitivity of this method is achievable through the use of the EIT phenomenon, facilitating optical detection of atomic interactions [16–19]. However, the presence of alkali-metal atoms on the inner surface of a vapor cell, due to a few layers of coating, induces non-zero conductivity in the glass [20]. This leads to an electric-field-screening effect, a consequence of photodesorption caused by laser irradiation at the cell’s surface [21, 22]. The phenomenon, originating from the induced internal electric field by ions, also occurred with cold atoms in high vacuum chambers [23–25]. Several strategies are available to counteract the induced electric field within the cell: (1) The utilization of externally connectable ring electrodes for applying electric fields within the cell [18]. (2) The insertion of film electrodes on the cell’s interior [22, 26]. (3) Rapid switching of the electric field [16]. (4) Direct application of UV light, Argon Laser, or heating to desorb surface metals [27–30]. (5) Three-photon excitation

with infrared laser fields [31]. The electric field screening effect allows for detecting high-frequency oscillating electric field signals ranging from MHz to THz. Notably, the technique can extend the detection spectrum of atomic electrometry, encompassing superlow-frequency (SLF) and extremely-low-frequency (ELF) bands, as well as static (dc) regions [19].

The detecting frequency of the atomic electrometry is limited by the time it takes for the induced electric field to respond to the external field. In principle, glass vapor cells are excellent electric insulators; however, the absorption of alkali-metal atoms leads to nonzero conductivity.

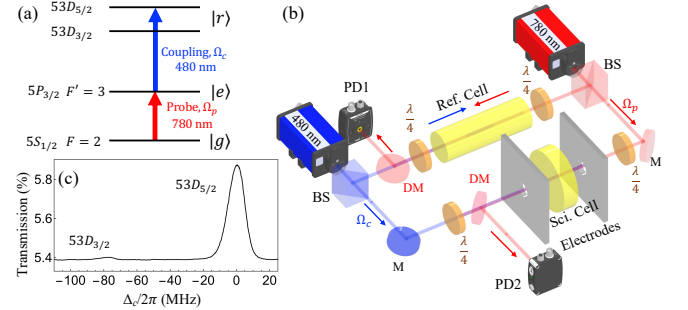


FIG. 1. (a) Energy levels of ^{87}Rb . The probe beam, with a wavelength of 780 nm, was frequency locked onto the transition from the ground state $|5S_{1/2}, F = 2\rangle$ to the excited state $|5P_{3/2}, F' = 3\rangle$. The coupling beam, with a wavelength of 480 nm, was swept to the transition from the excited state $|5P_{3/2}, F' = 3\rangle$ to the Rydberg states $53D_{3/2}$ and $53D_{5/2}$. The frequency difference between these two states is 78.3 MHz, used to calibrate the scanned frequency in a spectrum. (b) The schematic of the optical setup. The probe and coupling beams are counter-propagated, and their polarization is σ^+ . A reference cell is used for frequency calibration. Two stainless steel electrodes were attached on each side of the science cell, with a distance of 20 mm between them. A heating block made of aluminum is placed outside the electrodes. DM: dichroic mirror; $\lambda/4$: quarter wave plate; BS: cubed beam splitter; PD: photodetector. (c) Rydberg EIT spectrum without external electric field was measured using probe field transmission in the reference cell.

* yihsin.chen@mail.nsysu.edu.tw

We define the recovery time as the time that free charges redistribute the glass surface to maintain equal potential on the conductive surface when an external electric field is applied. The recovery time was 500 μs in Ref. [21] and it can be varied from 100 μs to 700 μs , depending on the coupling field intensity in Ref. [16]. A longer recovery time of 200 ms is reported in Ref. [17]. Our study utilizes Rydberg EIT resonances to characterize the cell's screening effect and charge dynamics as we vary parameters like E-field switching frequency, E-field amplitude, laser power, and vapor temperature. The recovery time varied from 0.7 ms to 450 ms and a low cutoff frequency below 10 Hz was successfully achieved. The results demonstrate significant progress in enhancing the performance of Rydberg atomic electrometry, offering valuable insights for future precision measurements and field sensing applications.

II. EXPERIMENTAL SETUP

We carried out the electric field measurement from an Rb vapor cell. The energy levels of ^{87}Rb involving Rydberg state and laser excitations are shown in Fig. 1. The probe beam, with a wavelength of 780 nm, was locked onto the transition from the ground state $|5S_{1/2}, F = 2\rangle$ to the excited state $|5P_{3/2}, F' = 3\rangle$ via the saturation absorption spectrum, which is not shown in the figure. Meanwhile, the coupling beam, with a wavelength of 480 nm, was either frequency scanned or locked to the transition of the excited state $|5P_{3/2}, F' = 3\rangle$ to the Rydberg state $53D_{5/2}$. The probe and coupling beams were counter-propagated through a reference cell and a science cell, and their polarizations were both σ^+ to achieve the maximum Rydberg EIT signal [32, 33]. These beams were collimated to a full width at e^{-2} maximum of 0.81 mm. To control the sheet resistance on the inner surface of the glass cell, we varied the coupling laser power from 2.4 mW to 14 mW and changed the probe laser power from 0.023 mW to 4.1 mW. The optimized probe power was 0.088 mW to achieve the highest EIT peak height [32]. The Rydberg EIT spectrum in Fig. 1(c) was obtained by measuring the transmission of the probe field in the absence of electric and magnetic fields in a reference cell. The scanned detuning was calibrated based on the frequency difference between $53D_{3/2}$ and $53D_{5/2}$ [34]. Using the EIT peak in the reference cell, we can compare the frequency shift caused by the external electric field.

We constructed an Rb vapor cell with a diameter of 25 mm flat windows. The thickness of the cell's windows is 3 mm, while the overall length of the cell is 19.2 mm (with a path length of 13.2 mm). The vacuum pressure was 2.2×10^{-7} torr before sealing the cell. The cell is made of borosilicate glass and filled with a natural abundance of Rb vapors. Two stainless steel electrodes were attached to each side of the cell. Two electrodes' dimensions are $50 \times 50 \text{ mm}^2$ to generate a uniform electric field in the laser propagation direction. We control

the electric field by a square waveform signal generated by a function generator. Laser beams are transmitted through electrode holes of 4 mm in diameter, with the electric field aligned parallel to the laser beams. An aluminum heating block is positioned adjacent to the electrodes. Optical density (OD) is a factor that increases the sensitivity of the EIT and the electrometry. It can be controlled by vapor temperature and determined by the probe field absorption signal at the resonance frequency. The cell temperature is set at 65°C or 75°C.

III. RESULTS

A scanned coupling field with a DC electric field was used to observe the Stark shift of the Rydberg thermal EIT spectrum. With an electric field of 1 V/cm, our theoretical calculation, using the Alkali Rydberg Calculator (ARC) PYTHON package [35], predicts the Stark shift of a few hundred MHz. However, we did not observe significant shift in the Rydberg EIT spectrum. The phenomenon may be induced by the screening effect. Rb coatings can be excited by the coupling field, which has a wavelength of 480 nm, so that the internal E-field induces shielding of the external E-field. In order to gain insights into the screening effect and charge dynamics within the cell, we then lock the coupling field to the peak transmission of Rydberg EIT and employ a square waveform to switch the electric field, as illustrated by the black line in Fig. 2. Subsequently, we detect the transmission signal from the probe field at resonant EIT, represented by the blue line. When a sufficiently high-frequency electric field is applied, specifically at 10 kHz in Fig. 2(a), the EIT transmission does not have enough time to respond to the electric field's rapid switching adequately. Therefore, the transmission experiences a sudden jump with opposite polarity compared to the electric field. Here we introduce the transient time, denoted as τ , which characterizes the duration for the EIT signal T decay to e^{-1} of its amplitude A , as expressed by an exponential function

$$T(t) = Ae^{-\frac{t}{\tau}} + y_0. \quad (1)$$

The probe field offset transmission, y_0 , indicates that the Stark shift occurs at steady state. The derived transient time is about few μs . When the switching frequency of the electric field exceeds the reciprocal of the transient time, the internal electric field fails to respond effectively. It constrains the upper boundary of the cutoff frequency within the range of MHz by this technique.

A vapor cell is generally made from a glass material that is an excellent electrical insulator. Glass can have non-zero conductivity due to the optically induced absorption of alkali-metal atoms on its interior surfaces. If the electric field is applied at a low frequency, e.g., 10 Hz, the EIT transmission suddenly jumps as shown in Fig. 2(b). Following each transmission jump, the EIT transmission took several tens of milliseconds to return to its original level. This indicates that the free charges

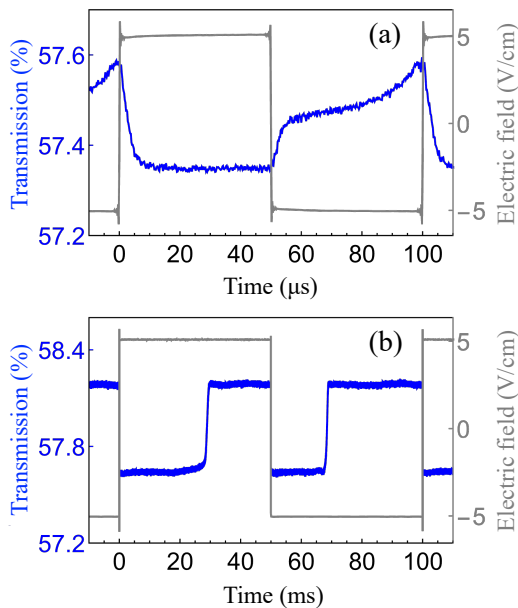


FIG. 2. Rydberg EIT peak signals varied under square waveform modulations of the electric field, with frequencies of 10 kHz in (a) and 10 Hz in (b). The electric field was generated by a function generator with $20 V_{pp}$, corresponding to the electric field of 10 V/cm. For fast modulation frequency, we derive the transient time of $2 \mu s$ from Eq. (1), which represents the time that the internal E field is influenced by the external E field. For slow modulation frequency, we derive the recovery times for the positive and negative E fields are 30 ms and 20 ms, respectively. The cell temperature was set to $65^\circ C$.

on the inner surface of the vapor cell redistribute over a certain timescale, defined as the recovery time, leading to an equal electric potential on the surface and shielding of the external electric field. Take the measurement in Fig. 2(b) as an example. When the electric field is positive, the recovery time measured at 30 ms is longer than when the electric field is negative, which is 20 ms. Detailed discussion about the effect of the recovery time can be found in Sec. IV.

To ensure that the electric field induces Stark shift and influences the Rydberg EIT, we simultaneously switched the electric field while sweeping the coupling field across $|53D_{5/2}\rangle$ Rydberg state. Figures 3(a), 3(b), and 3(c) are the spectra with the E-field modulation frequencies of 1 kHz, 100 Hz, and 10 Hz. For 10-Hz data (in 3(c)), the coupling field scanning time was increased tenfold to improve clarity. In the presence of an external E field, the Rydberg EIT energy shifts from resonance, resulting in a two-level absorption, subsequently causing a reduction in the EIT signal. In the case of fast modulation, e.g., faster than 100 Hz, the induced energy shift cannot return to its original state in time, so the EIT signals have the opposite polarity compared to the E-field signal. Consequently, the Rydberg EIT spectrum exhibits a square modulation. When the duty cycle of the EIT

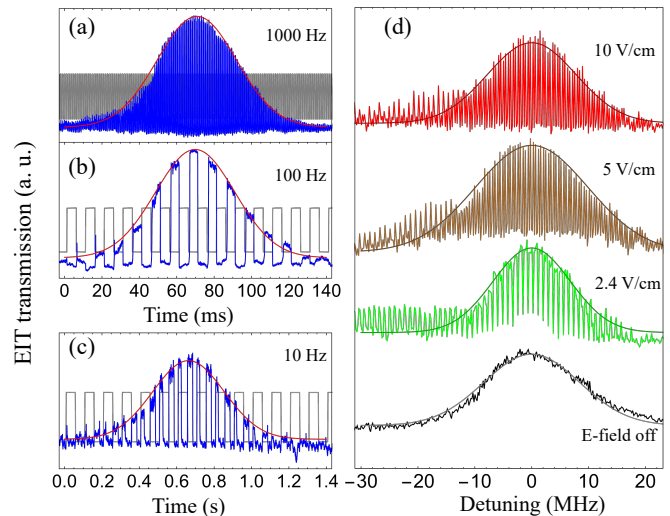


FIG. 3. Rydberg EIT spectra with E-field modulation of 1 kHz (a), 100 Hz (b), and 10 Hz (c). The coupling field frequency was scanned across the $53D_{5/2}$ Rydberg state. Gray lines represent the E-field signals. For sufficiently fast E-field modulations, e.g., faster than 100 Hz (Fig. 3(b)), the EIT signals have the opposite polarity compared to the E-field signals. For 10-Hz data, the coupling field scanning time was increased by tenfold to improve clarity. (d) Rydberg EIT spectra with 1 kHz E-field modulation and 10, 5, 2.4, 0 V/cm E-field strength from top to bottom.

signal is approximately 50%, such as with a 10 Hz E-field modulation, it limits the lower boundary cutoff frequency attainable using this technique. Figure 3(d) shows the Rydberg EIT spectra with 1 kHz E-field modulation and varied field strength. Solid lines are Gaussian fits to EIT resonance envelopes. With the intensity of 10 V/cm, the linewidth was broadened due to the asymmetrical or non-uniform generation of charges within the cell, forming of an inhomogeneous electric field. Besides the square modulation on Rydberg resonance, the Stark effect is also visible at a detuning of 0 to -30 MHz with long tail EIT signals above the Gaussian fitting lines. EIT resonance shifts to the same sign because of quadratic electric field dependence, $\delta \propto E^2$.

In extremely low-frequency bands (ELFs), Rydberg atomic electrometry presents an extremely promising method for measuring external electric fields. We employ the fast Fourier transform (FFT) analysis with a Blackman-Harris window to examine the frequency components of the external field derived from the modulated Rydberg EIT signals. The FFT spectra, depicted in the main and inset plots of Fig. 4(a), have a span of 1.5 kHz and 1 Hz, respectively. This technique can determine E-field modulation at 1 kHz with a resolution of up to 10 mHz. The presence of the 60 Hz ambient signal is evident, while the additional peak observed can be attributed to the square wave modulation. Subsequently, the E-field modulation was adjusted to 10 Hz. The FFT signals, which remained distinctly observable, highlight

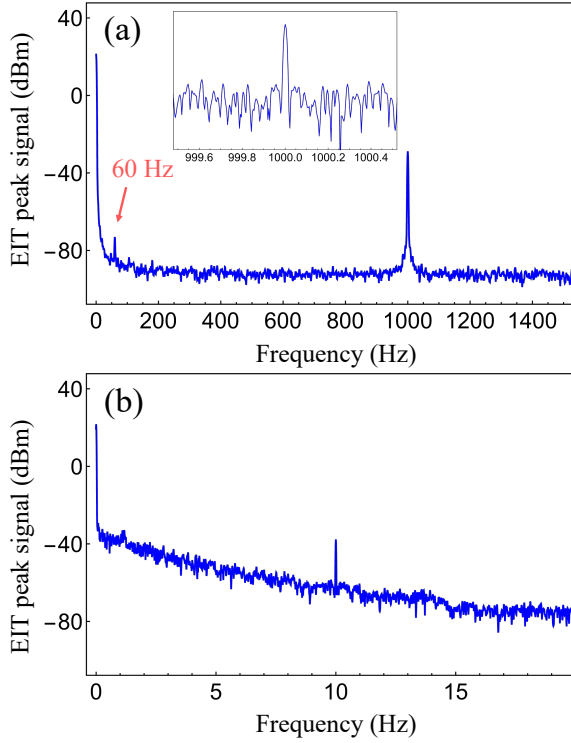


FIG. 4. FFT analysis with Blackman-Harris window to examine the frequency components of the external field derived from the Rydberg EIT peak signals under square modulation. The modulation frequencies of the E field were 1 kHz in (a) and 10 Hz in (b) with square-waveform voltage signals. The span in the main and inset plots are 1.5 kHz and 1 Hz in (a), and that is 20 Hz in (b). The AC power with a frequency of 60 Hz is also shown in (a). The inset spectrum shows that the frequency resolution is 10 mHz. In (b), the 10 Hz E-field modulation exhibits a distinct signal that remains evident. This technique enables the low-frequency sensor to achieve high sensitivity.

the sensitivity of the low-frequency sensor. Note that employing sinusoidal waves for the external electric field at low frequencies prevents the internally induced electric field from effectively canceling the external disturbances, primarily due to its slow response. Thus, the utilization of square modulation enables the electric field sensor to be functional at lower frequencies. However, the detection of higher frequencies is constrained by the transient time, as mentioned in Eq. (1). This study shows the transient times were from 1 to 10 μ s, with minor fluctuations attributed to vapor temperature and major variations correlated with EIT peak signals. These variations establish an upper limit of 1 MHz for the detected frequency using this technique. Thus, our study reveals a standard quantum limit for data capacity and experimentally illustrates it across bandwidths from 10 Hz to 1 MHz.

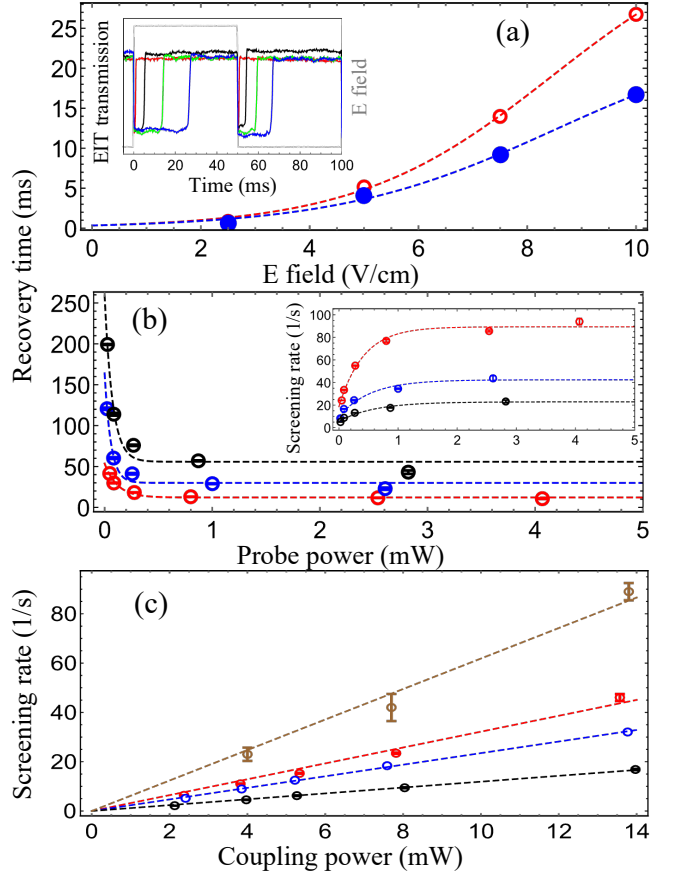


FIG. 5. The recovery times with varied electric field strength in (a) and varied probe power in (b). The screening rate (reciprocal of the recovery time) with varied probe power in the inset of (b) and varied coupling power in (c). Red-open circles and blue-solid circles in (a) are the recovery times when the electric field is turned on in the positive and negative direction, respectively. The dashed lines are the fitting line with a growth logistic function. In (a), the probe and coupling powers were 0.16 mW and 13.8 mW (the strongest coupling power we applied in this study). In (b), the coupling power was 14 mW (red circles), 7.7 mW (blue), and 4.0 mW (black); and in (c), the probe power was 280 μ W (red), 86 μ W (blue), and 27 μ W (black). The brown data represent the saturation screening rate γ_0 from the inset of (b). The E-field was set as 10 V/cm in both (b) and (c).

IV. DISCUSSION

The lowest frequency detection of Rydberg atomic electrometry is limited by the recovery time of the shielding. The recovery time is the time that free charges redistribute the glass surface to maintain equal potential on the conductive surface when an external electric field is applied. We further investigate the parameters that govern the recovery time. First, we adjust the E-field strength under the probe and coupling powers of 0.16 and 13.8 mW. The extracted recovery times are shown in Fig. 5(a), and they can be fitted by a growth logistic

function, $\frac{t_{sat}}{1+e^{-(E-E_0)/\tau_E}}$. Based on the growth behavior, it appears that the electron concentration increases as the electric field strength increases, leading to an interplay between carrier generation, mobility, and interactions in response to external fields. Mobility refers to how easily electrons can move through the glass surface when subjected to an electric field. The presence of a strong electric field can enhance the mobility of charge carriers, allowing them to move more easily through the material, leading to more efficient charge transport and accumulation. The application of a strong electric field prolongs the recovery time due to significant energy level shifts and disturbances to the internal electric field. The scaling factor τ_E denotes the average electric field strength, influencing the logistic growth rate or the steepness of the curve. Smaller values of τ_E imply that a smaller change in the electric field is required to increase the charge number. The red-open circles and blue-solid circles in Fig. 5(a) are the recovery times at the positive and negative electric field transition, respectively. The values of τ_E are 1.8 V/cm and 2.0 V/cm for the red and blue data, respectively. According to the measurements, the ratio of the recovery times between positive and negative E fields was approximately 1.5, likely attributed to an inhomogeneous E field generated by the electrodes. This has been confirmed by exchanging the direction of E field in space. Thus, we will only discuss the analysis when the E field is in the positive direction in the following discussion. There are physical limitations or saturation effects that affect recovery time. For instance, as the electron concentration increases, interactions between electrons could lead to recombination processes that limit further growth.

We then adjust the probe and coupling powers and extract the recovery time under an E field of 10 V/cm, as shown in Figs. 5(b) and 5(c). When the probe power increases, more photons collide with free electrons, leading to faster equilibration of the electrons, i.e., shorter recovery time. Here, we define the screening rate of the electric field as the reciprocal of the recovery time. In Fig. 5(b), the coupling powers were 14 mW (red circles), 7.7 mW (blue), and 4.0 mW (black). With the presence of the coupling laser, higher probe power leads to a higher screening rate, but it is not linear. Screening rates exponentially increase with probe power and become saturated at a certain value. Dashed lines indicate the best fit using the function $A \cdot \text{Exp}[-P_p/\tau_p] + \gamma_0$, where A is a constant, and P_p is the probe power. The saturation screening rates, denoted as γ_0 , are 89, 42, and 23 (1/s), with corresponding τ_p values of 0.37, 0.54, and 0.60 mW for the strongest to the weakest coupling power. The saturation screening rate, reflecting the photoelectric current in the photoelectric effect, is predominantly influenced by the coupling laser power (480 nm). τ_p serves as a parameter representing the characteristic constant associated with the photoelectric current's response to the probe laser power. A smaller τ_p implies a faster response of the photoelectric current to change in laser

power. Therefore, stronger laser powers result in faster screening rates, corresponding to shorter recovery times.

Next, we investigate the relationship between the screening rate and coupling power while keeping the probe power constant. In Fig. 5(c), the screening rate demonstrates a linear increase with the coupling power, maintaining fixed probe powers of 280 μ W (red circles), 86 μ W (blue), and 27 μ W (black). The brown data represent the saturation screening rate γ_0 from the inset of Fig. 5(b). The corresponding slopes are 6.2, 3.2, 2.4, and 1.2 (1/s/mW) from top to bottom. This observation substantiates that the screening rate of excited Rb atoms is influenced by the 780 nm probe laser and the 480 nm coupling laser. In principle, the 780 nm photon may not be sufficient to cause electronic transitions within the solid-state Rb metal directly. However, the absorption of the 780 nm light may result in localized effects. As the rubidium metals, encompassing both isotopes, absorb the laser, they transfer energy to the electrons, increasing their kinetic energy in the localized region. Consequently, free electrons can readily escape from the surface when exposed to the 480 nm photons. It is also the phenomenon of light-induced atom desorption (LIAD), which has been used as a tool to flexibly control the atomic density [27, 28]. A short wavelength light source allows fast switching of the desired vapor pressure. The recovery time can be varied from 1 ms to 400 ms by adjusting the laser powers. Therefore, the frequency detection of Rydberg atomic electrometry can cover the extremely-low-frequency (ELF) band.

V. CONCLUSION AND OUTLOOK

Our experiments in a Rb vapor cell illustrate the effectiveness of low-frequency atomic electrometry through Rydberg EIT measurements. We successfully identified the screening effect induced by external electric fields and Rydberg excitation, clarifying its origin in the charge dynamics resulting from the photoelectric effect of the Rb coating under the influence of the probe and coupling beams. Utilizing FFT analysis on the E-field modulated Rydberg EIT signals, we demonstrated the capability to measure frequency electric fields from 10 Hz to 1 MHz. The frequency detection range of this Rydberg atomic electrometry is constrained by the recovery and transition times of the shielding process. Our systematic study revealed that adjusting the probe and coupling field power, as well as the E-field strength, can influence the recovery time and screening rate. Remarkably, this atomic electrometry extends its applicability to the extremely-low-frequency (ELF) band, presenting a promising technique for sensitively measuring low-frequency electric fields. This expansion enhances its versatility across various fields, allowing for the detection of electric fields originating outside the vacuum environment over a broader range.

ACKNOWLEDGMENTS

This work was supported by Grants Nos. 112-2112-M-110-008 and 112-2123-M-006-001 of the National Science and Technology Council, Taiwan. The authors thank Prof. Tsu-Chiang Yen for the valuable comments on the study.

-
- [1] T. F. Gallagher, *Rydberg Atoms*, Cambridge Monographs on Atomic, Molecular and Chemical Physics (Cambridge University, 1994).
- [2] T. Vogt, M. Viteau, J. Zhao, A. Chotia, D. Comparat, and P. Pillet, Dipole Blockade at Förster Resonances in High Resolution Laser Excitation of Rydberg States of Cesium Atoms, *Phys. Rev. Lett.* **97**, 083003 (2006).
- [3] M. Saffman, T. G. Walker, and K. Mølmer, Quantum information with Rydberg atoms, *Rev. Mod. Phys.* **82**, 2313 (2010).
- [4] D. Jaksch, J. I. Cirac, P. Zoller, S. L. Rolston, R. Côté, and M. D. Lukin, Fast Quantum Gates for Neutral Atoms, *Phys. Rev. Lett.* **85**, 2208 (2000).
- [5] L. Isenhower, M. Saffman, and K. Mølmer, Multibit C_k NOT quantum gates via Rydberg blockade, *Quantum Inf. Process.* **10**, 755 (2011).
- [6] H. Gorniaczyk, C. Tresp, J. Schmidt, H. Fedder, and S. Hofferberth, Single-Photon Transistor Mediated by Interstate Rydberg Interactions, *Phys. Rev. Lett.* **113**, 053601 (2014).
- [7] D. Tiarks, S. Baur, K. Schneider, S. Dürr, and G. Rempe, Single-Photon Transistor Using a Förster Resonance, *Phys. Rev. Lett.* **113**, 053602 (2014).
- [8] D. Tiarks, S. Schmidt-Eberle, T. Stolz, G. Rempe, and S. Dürr, A photon–photon quantum gate based on Rydberg interactions, *Nat. Phys.* **15**, 124 (2019).
- [9] I. I. Ryabtsev, D. B. Tretyakov, I. I. Beterov, and V. M. Entin, Observation of the Stark-Tuned Förster Resonance between Two Rydberg Atoms, *Phys. Rev. Lett.* **104**, 073003 (2010).
- [10] S. Ravets, H. Labuhn, D. Barredo, L. Béguin, T. Lahaye, and A. Browaeys, Coherent dipole–dipole coupling between two single Rydberg atoms at an electrically-tuned Förster resonance, *Nat. Phys.* **10**, 914 (2014).
- [11] S. Ravets, H. Labuhn, D. Barredo, T. Lahaye, and A. Browaeys, Measurement of the angular dependence of the dipole-dipole interaction between two individual Rydberg atoms at a Förster resonance, *Phys. Rev. A* **92**, 020701(R) (2015).
- [12] C.-E. Wu, T. Kirova, M. Auzins, and Y.-H. Chen, Rydberg-Rydberg interaction strengths and dipole blockade radii in the presence of Förster resonances, *Opt. Express* **31**, 37094 (2023).
- [13] S. Sevinçli and T. Pohl, Microwave control of Rydberg atom interactions, *New Journal of Physics* **16**, 123036 (2014).
- [14] D. B. Tretyakov, V. M. Entin, E. A. Yakshina, I. I. Beterov, C. Andreeva, and I. I. Ryabtsev, Controlling the interactions of a few cold Rb Rydberg atoms by radio-frequency-assisted Förster resonances, *Phys. Rev. A* **90**, 041403(R) (2014).
- [15] S. de Léséleuc, D. Barredo, V. Lienhard, A. Browaeys, and T. Lahaye, Optical Control of the Resonant Dipole-Dipole Interaction between Rydberg Atoms, *Phys. Rev. Lett.* **119**, 053202 (2017).
- [16] A. K. Mohapatra, T. R. Jackson, and C. S. Adams, Coherent Optical Detection of Highly Excited Rydberg States Using Electromagnetically Induced Transparency, *Phys. Rev. Lett.* **98**, 113003 (2007).
- [17] Y.-Y. Jau and T. Carter, Vapor-Cell-Based Atomic Electrometry for Detection Frequencies below 1 kHz, *Phys. Rev. Appl.* **13**, 054034 (2020).
- [18] L. Ma, M. A. Viray, D. A. Anderson, and G. Raithel, Measurement of dc and ac Electric Fields inside an Atomic Vapor Cell with Wall-Integrated Electrodes, *Phys. Rev. Appl.* **18**, 024001 (2022).
- [19] L. Li, Y. Jiao, J. Hu, H. Li, M. Shi, J. Zhao, and S. Jia, Super low-frequency electric field measurement based on Rydberg atoms, *Opt. Express* **31**, 29228 (2023).
- [20] Y.-C. Chen, S.-C. Fang, H.-H. Lin, J.-W. Dong, and Y.-H. Chen, Investigation of alkali vapor diffusion characteristics through microchannels, *Phys. Fluids* **34**, 072004 (2022).
- [21] K. C. Cox, D. H. Meyer, F. K. Fatemi, and P. D. Kunz, Quantum-Limited Atomic Receiver in the Electrically Small Regime, *Phys. Rev. Lett.* **121**, 110502 (2018).
- [22] D. Barredo, H. Kübler, R. Daschner, R. Löw, and T. Pfau, Electrical Readout for Coherent Phenomena Involving Rydberg Atoms in Thermal Vapor Cells, *Phys. Rev. Lett.* **110**, 123002 (2013).
- [23] J. M. McGuirk, D. M. Harber, J. M. Obrecht, and E. A. Cornell, Alkali-metal adsorbate polarization on conducting and insulating surfaces probed with Bose-Einstein condensates, *Phys. Rev. A* **69**, 062905 (2004).
- [24] R. P. Abel, C. Carr, U. Krohn, and C. S. Adams, Electrometry near a dielectric surface using Rydberg electromagnetically induced transparency, *Phys. Rev. A* **84**, 023408 (2011).
- [25] M. Viteau, J. Radogostowicz, M. G. Bason, N. Malossi, D. Ciampini, O. Morsch, and E. Arimondo, Rydberg spectroscopy of a Rb MOT in the presence of applied or ion created electric fields, *Opt. Express* **19**, 6007 (2011).
- [26] R. Daschner, H. Kübler, R. Löw, H. Baur, N. Frühauf, and T. Pfau, Triple stack glass-to-glass anodic bonding for optogalvanic spectroscopy cells with electrical feedthroughs, *Appl. Phys. Lett.* **105**, 041107 (2014).
- [27] E. B. Alexandrov, M. V. Balabas, D. Budker, D. English, D. F. Kimball, C.-H. Li, and V. V. Yashchuk, Light-induced desorption of alkali-metal atoms from paraffin coating, *Phys. Rev. A* **66**, 042903 (2002).
- [28] C. Klempt, T. van Zoest, T. Henninger, O. Topic, E. Rasel, W. Ertmer, and J. Arlt, Ultraviolet light-induced atom desorption for large rubidium and potas-

- sium magneto-optical traps, *Phys. Rev. A* **73**, 013410 (2006).
- [29] J. A. Sedlacek, E. Kim, S. T. Rittenhouse, P. F. Weck, H. R. Sadeghpour, and J. P. Shaffer, Electric Field Cancellation on Quartz by Rb Adsorbate-Induced Negative Electron Affinity, *Phys. Rev. Lett.* **116**, 133201 (2016).
- [30] P. Anderson, S. Jalnapurkar, E. S. Moiseev, D. Chang, P. E. Barclay, A. Lezama, and A. I. Lvovsky, Optical nanofiber temperature monitoring via double heterodyne detection, *AIP Advances* **8**, 055005 (2018).
- [31] M. J. Lim, M. Cervantes, C. Brady, S. McPoyle, and J. Simmermon, Kilohertz-range electric field calibration in an alkali vapor cell using time-averaged Stark shifts, *Applied Physics Letters* **123**, 051106 (2023).
- [32] H.-J. Su, J.-Y. Liou, I.-C. Lin, and Y.-H. Chen, Optimizing the Rydberg EIT spectrum in a thermal vapor, *Opt. Express* **30**, 1499 (2022).
- [33] H.-J. Su, J.-Y. Liou, I.-C. Lin, and Y.-H. Chen, Optical pumping effects on high-contrast rydberg electromagnetically induced transparency, *J. Appl. Phys.* **132**, 244401 (2022).
- [34] M. Mack, F. Karlewski, H. Hattermann, S. Höckh, F. Jessen, D. Cano, and J. Fortágh, Measurement of absolute transition frequencies of ^{87}Rb to nS and nD Rydberg states by means of electromagnetically induced transparency, *Phys. Rev. A* **83**, 052515 (2011).
- [35] N. Šibalić, J. D. Pritchard, C. S. Adams, and K. J. Weatherill, ARC: An open-source library for calculating properties of alkali Rydberg atoms, *Computer Physics Communications* **220**, 319 (2017).